Zhu et al. PhotoniX (2025) 6:17
https://doi.org/10.1186/s43074-025-00176-5

PhotoniX

RESEARCH

Open Access

High-speed optical coherence manipulation based on lithium niobate films modulator

Xinlei Zhu[1], Fengchao Ni[2], Haigang Liu[2], Jiayi Yu[1], Fei Wang[3], Ya Cheng[4*], Xianfeng Chen[2*] and Yangjian Cai[1*]

*Correspondence:
ya.cheng@siom.ac.cn;
xfchen@sjtu.edu.cn;
yangjiancai@sdnu.edu.cn

[1] Shandong Provincial Engineering and Technical Center of Light Manipulation and Shandong Provincial Key Laboratory of Optics and Photonic Devices, School of Physics and Electronics, Shandong Normal University, Jinan 250358, China
[2] State Key Laboratory of Advanced Optical Communication Systems and Networks, School of Physics and Astronomy, Shanghai Jiao Tong University, Shanghai 200240, China
[3] School of Physical Science and Technology, Soochow University, Suzhou 215006, China
[4] XXL-The Extreme Optoelectromechanics Laboratory, School of Physics and Electronics Science, East China Normal University, Shanghai 200241, China

Abstract

Research on the optical coherence manipulation has made significant progress, but the modulation rate of conventional tailoring technology is too low, which has become a key factor hindering its transition from laboratory to practical application. Here, we utilize lithium niobate films (LNF) modulator to achieve high-speed optical coherence manipulation based on its high-speed electro-optical modulation capability. Our experimental modulation rate reaches 350 kHz, which is about 20 times higher than the fastest modulation rate reported so far. This design strategy provides a simple rule for high-speed optical coherence manipulation based on electro-optical modulation, paving the way for further practical applications of optical coherence manipulation technology.

Keywords: Optical coherence, Lithium niobate films, High-speed manipulation, Random field, Statistical property

Introduction

Spatially structured light refers to the arbitrary tailoring of its spatial degrees of freedom, encompassing spatial characteristics such as amplitude, phase, and polarization, and has been proven to have application value [1–3]. Light field manipulation is traditionally based on fully coherent optics approaches. However, it is known that the light beams produced by these methods introduce some negative effects, such as speckle noise [4], and are very sensitive to external perturbations [5]. Mitigating this vulnerability has been an open challenge and requires in-depth research. Optical coherence is another important fundamental characteristic of light field, which is determined by statistical optical property and plays an important role in tailoring light fields and understanding light-matter interactions [6]. A large number of studies have shown that optical coherence manipulation can not only endow light fields with many extraordinary physical features, but also greatly reduce negative effects such as speckle noise and field degradation caused by random media [7]. It has broad application prospects in optical imaging, optical encryption, optical tweezers and other fields [8–15].

Although significant progress has been made in optical coherence manipulation research, the modulation rate of traditional manipulation technology is too low to be applied in practice, for example, optical communications require modulation rates from gigahertz to terahertz. Optical coherence manipulation methods are mainly based on the van Cittert-Zernike theorem [16] and the coherent-mode representation theorem [17]. The former usually requires the use of a liquid crystal spatial light modulator or a digital micromirror device to produce prescribed incoherent light, resulting in the modulation rate being limited to 60 Hz and 17 kHz, respectively, and it can only customize Schell-model coherent structures. For the latter, due to the diversity of coherence modes and superposition methods, this method has flexible and rich tailoring capabilities; however, this method still requires the use of the above two optical modulators, and still does not solve the problem of too low modulation rate [7]. The latest research reports that spatial coherence manipulation can be achieved with the aid of optical metasurfaces [18], but this method still has the problem of too low modulation rate. Therefore, to realize practical applications based on optical coherence manipulation, a key scientific issue needs to be solved, namely, how to achieve high-speed optical coherence manipulation.

Lithium niobate (LN) material has always been the first choice for high-speed electro-optic modulation materials due to its excellent linear electro-optic effect (Pockels effect) [19]. In recent years, with the maturity of lithium niobate films (LNF) preparation technology, high-quality LN single crystalline films have been commercialized. It not only retains the superior characteristics of LN crystal, but also can better constrain the light field and reduce power consumption due to the large refractive index difference between LN and silicon dioxide. Stimulated by the excellent nonlinear optical and electro/acousto-optic properties of LN and the maturing advancement of microfabrication technique, a plethora of integrated photonic devices on the LNF on insulator platform have been investigated. Most electric beam deflectors [20] and optical modulators [21–23] are proposed based on the LN platform. Furthermore, by applying voltage to the LN waveguide, the phase distribution of the light field can be precisely and quickly controlled, which opens the possibility of tailoring optical coherence using LNF modulator. In this paper, we introduce a novel application of LNF modulators for optical coherence manipulation. By designing specific modulation voltages, we achieve precise, high-speed control of the light field's phase distribution and tailor optical coherence through the superposition of multiple coherence modes. Our experimental results are consistent with theoretical predictions, and the proposed strategy can also be easily extended to tailor the optical coherence of different special light fields. This strategy paves the way for practical applications of optical coherence tailoring.

Results

Manipulation principle

Random fields belong to electromagnetic fields, which are solutions to Maxwell's equations and show partial coherence in the space-time domain or the space-frequency domain. A random field with prescribed statistical properties can be represented by a sample function extracted from a random process described by a correlation function. Considering a scalar physical electric field $E(\mathbf{r}, t) = U(\mathbf{r}, t)\exp(-i2\pi\bar{\omega}t)$, with $\mathbf{r}$ is the two-dimensional transverse coordinate, $\bar{\omega}$ is the mean frequency. Assuming that $U(\mathbf{r}, t)$ changes slowly with time t respect to the complex carrier $\exp(-i2\pi\bar{\omega}t)$. Therefore, $U(\mathbf{r}, t)$ is a slowly changing random field with a complex envelope function. For more brevity, we assume that the field is wide-sense stationary and omit the dependence of subsequent physical quantities on t and ω, and set the random field $U(\mathbf{r})$ as

$$U(\mathbf{r}) = \sqrt{S(\mathbf{r})} \exp\left[i\varphi(\mathbf{r})\right], \tag{1}$$

with $S(\mathbf{r})$ and $\varphi(\mathbf{r})$ represent the spectral density and phase of the random field instance, respectively.

The statistical properties of a random field are represented by the second-order field moment. The ensemble of all random fields is called the cross-spectral density function, which can also be viewed as an incoherent superposition of many statistically independent coherent modes [17]

$$\left\langle U(\mathbf{r}_1)U^*(\mathbf{r}_2)\right\rangle = W(\mathbf{r}_1, \mathbf{r}_2) = \sum_{n=1}^{N} \Psi_n(\mathbf{r}_1)\Psi_n^*(\mathbf{r}_2), \tag{2}$$

where $\{\Psi_n(\mathbf{r})\}_N$ represent a set of incoherent modes with the sequence number n and the total number N. To separate the spectral density characteristics and coherence characteristics of the random fields, the cross-spectral density function is normalized and defined as the spectral degree of coherence [24]

$$\mu(\mathbf{r}_1, \mathbf{r}_2) = \frac{W(\mathbf{r}_1, \mathbf{r}_2)}{\sqrt{S(\mathbf{r}_1)S(\mathbf{r}_2)}}. \tag{3}$$

where $S(\mathbf{r}) = W(\mathbf{r}, \mathbf{r})$ is the spectral density. From Eqs. (1)–(3), we obtain the spectral degree of coherence at two arbitrary points

$$\mu(\mathbf{r}_1, \mathbf{r}_2) = \left\langle \exp\left[i\varphi(\mathbf{r}_1) - i\varphi(\mathbf{r}_2)\right]\right\rangle. \tag{4}$$

According to this, the coherence characteristics of random fields are essentially determined by the phase distribution, which means that optical coherence manipulation can be achieved by designing a prescribed phase distribution, and modulators with high-speed phase modulation capability can achieve high-speed optical coherence manipulation.

Lithium niobate films modulator

We take advantage of the high-speed electro-optical modulation capability of LNF and design a one-dimensional array LNF modulator with 64 independent modulation channels and a binary modulation rate of 2 MHz. The device structure and operating mode are illustrated in Fig. 1a, where the upper-left corner shows a photo of the actual device, and the bottom-left corner displays a magnified image of the device (5× zoom). The device structure mainly includes three parts: a gold electrode array, a Z-cut LNF, and a gold electrode backplate. The gold electrode backplate is used for grounding and forms a plate capacitor with the gold electrode array, Fig. 1b presents a schematic of the device structure, with an electrode width of 140 μm. When different voltages are applied to different electrode channels of the LNF modulator, the light waves produce a prescribed wavefront distribution due to the difference in refractive index they produce. In addition, in order to ensure low coupling loss of the LNF modulator and improve energy utilization (the coupling efficiency

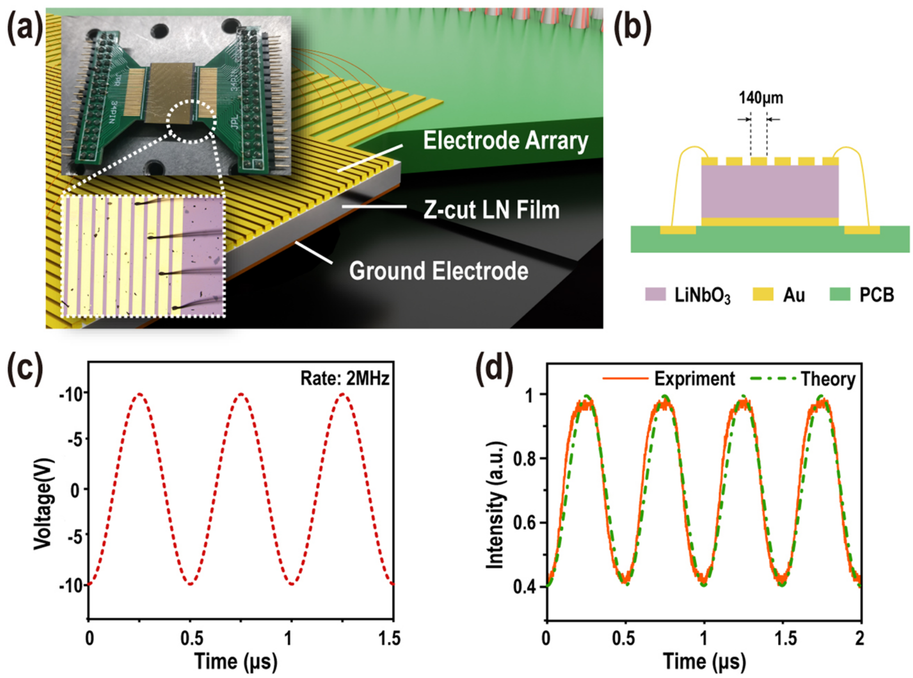

Fig. 1 Lithium niobate films modulator. **a** Design of the LNF Modulator, the device (top left) and detailed image magnified five times (lower left); **b** Structural diagram of the top electrode; **c** Temporal characteristics of the driving voltage. **d** Normalized intensity of the modulation light response to 2 MHz driving voltage

of our device is about 49%), the thickness of LNF is determined to be 100 μm, and the length of the channel is 2 cm. The designed LNF modulator is driven by multiple synchronous analog signals output from the data acquisition card. The driving voltage and phase change satisfy

$$\varphi = \frac{\pi n_e^3 \gamma_{33} L V}{\lambda d}, \tag{5}$$

where n_e is the refractive index for the e-light, γ_{33} is the electro-optic coefficients of LN, L is the length of the LNF modulator, V is the applied external voltage, d is the thickness of the LNF, and λ is the wavelength of the input laser beam. When linearly polarized light is vertically incident on the LNF modulator, higher phase modulation depth can be achieved. Figure 1c and d shows temporal characteristics of the driving voltage and normalized intensity of the modulation light response to 2 MHz driving voltage, which are highly consistent with the experimental results, demonstrating that a binary modulation rate of 2 MHz can be achieved based on the LNF modulator. It should be noted that the overall modulation rate is primarily limited by the charging and discharging time of the plate capacitor composed of gold electrodes. Potential strategies for improvement include reducing the lateral dimensions of the electrodes to lower capacitance, employing LN micro- or nanofilms to fabricate integrated devices, and minimizing the overall device size to achieve higher modulation rates. A more detailed description of the fabrication processes of high-speed LNF modulator is given in Supplementary Note 1.

Optical coherence manipulation

In order to verify the high-speed optical coherence manipulation capability of the LNF modulator, a one-dimensional Gaussian Schell-model source is selected as an experimental case. Its cross-spectral density function is expressed as $W(\mathbf{r}_1, \mathbf{r}_2) = \tau(\mathbf{r}_1)\tau^*(\mathbf{r}_2)\mu(x_1, x_2)$, where $\tau(\mathbf{r})$ is the amplitude that satisfies the Gaussian distribution, and the one-dimensional degree of coherence $\mu(x_1, x_2)$ is expressed as [25]

$$\mu(x_1, x_2) = \exp\left[-(x_2 - x_1)^2/2\delta^2\right], \tag{6}$$

here, δ represents the coherence width in the x-direction. According to the coherent-mode representation theorem, random light fields can be generated by the incoherent superposition of coherent modes sets $\{\Psi_n(\mathbf{r})\}$. Figure 2 shows a diagram of the coherent-mode representation of random fields. A set of random phases $\{\varphi_n(\mathbf{r})\}$, shown in Fig. 2a is extracted from the coherent modes set $\{\Psi_n(\mathbf{r})\}$ and applied to a determined field to randomly modulate the wavefront of the output beam, thereby statistically obtaining a random light source with prescribed coherence distribution. Figure 2b shows the spectral density distribution and the one-dimensional spectral degree of coherence distribution of one-dimensional Gaussian Schell-model source under different coherence widths. According to Eq. (2), the independent coherence mode of the one-dimensional Gaussian Schell-model source can be expressed as

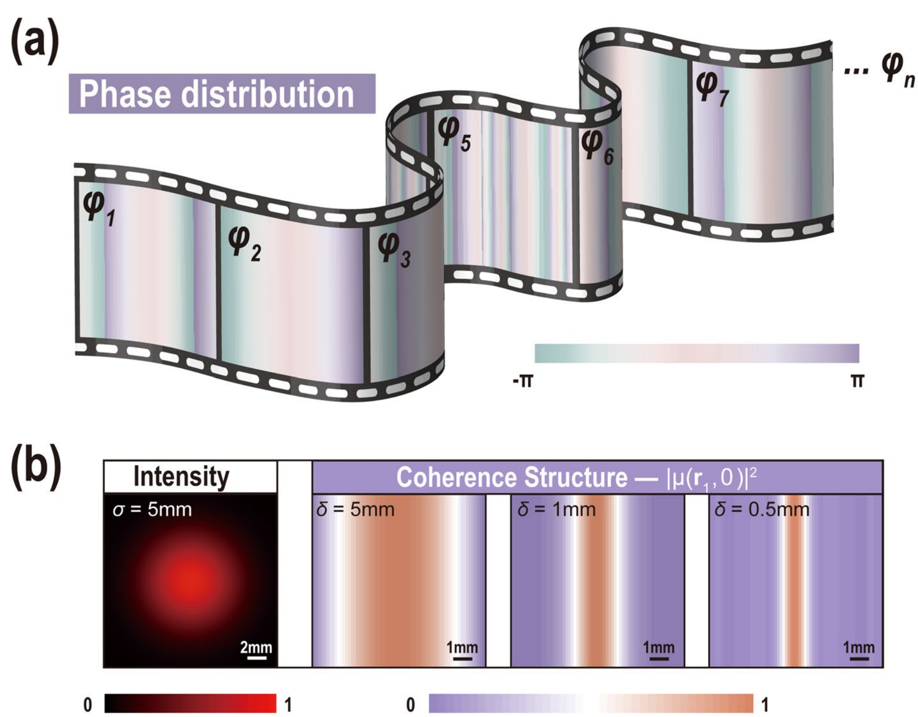

Fig. 2 Principle and diagram of modal decomposition of a random field. **a** A set of phase distribution set $\{\varphi_n(\mathbf{r})\}$ of coherent modes $\{\Psi_n(\mathbf{r})\}$; **b** The spectral density distribution and spectral degree of coherence distribution of a one-dimensional Gaussian Schell-model source under different coherence widths

$$\Psi_n(\mathbf{r}) = \left(\sqrt{2\pi}\delta\Delta\nu\right)^{1/2} \exp\left(-\mathbf{r}^2/2\sigma^2 - \sqrt{2}\pi\delta\nu_n - 2\pi ix\nu_n\right), \tag{7}$$

where σ is the initial beam waist, and $\Delta\nu$ is the intervals of the discrete integral equation. Therefore, a one-dimensional Gaussian Schell-model source can be viewed as an incoherent superposition of coherent Gaussian modes controlled by different linear phases. Further details regarding the phase control can be found in Supplementary Note 2.

Experimental setup

As shown in Fig. 3a, the laser with a wavelength of 671 nm (within the modulator's operating range of 0.4μm to 5μm) and linear polarization in the y-direction passes through a cylindrical lens (CL1) and is vertically coupled into the LNF modulator. The output beam is collimated by another cylindrical lens (CL2). Driving signals corresponding to the set of coherent Gaussian modes $\{\Psi_n(\mathbf{r})\}$ are applied on all electrodes of the LNF modulator, and the total number of sufficient modes extracted is $N = 625$, which has been demonstrated in previous report [26]. The CCD records the instantaneous intensity produced by each alteration in the wavefront phase. Figure 3b shows the average intensity of the modulated source which is calculated from the ensemble average of 625 instantaneous intensities. It should be emphasized that due to the hardware limitations of the data acquisition card, the modulation frequency of the LNF modulator in the $0 \sim 2\pi$ phase distribution range is 350 kHz. Considering the modulation rate of the LNF modulator itself (2 MHz), it is nearly a hundred times higher than the binary phase refresh rate of

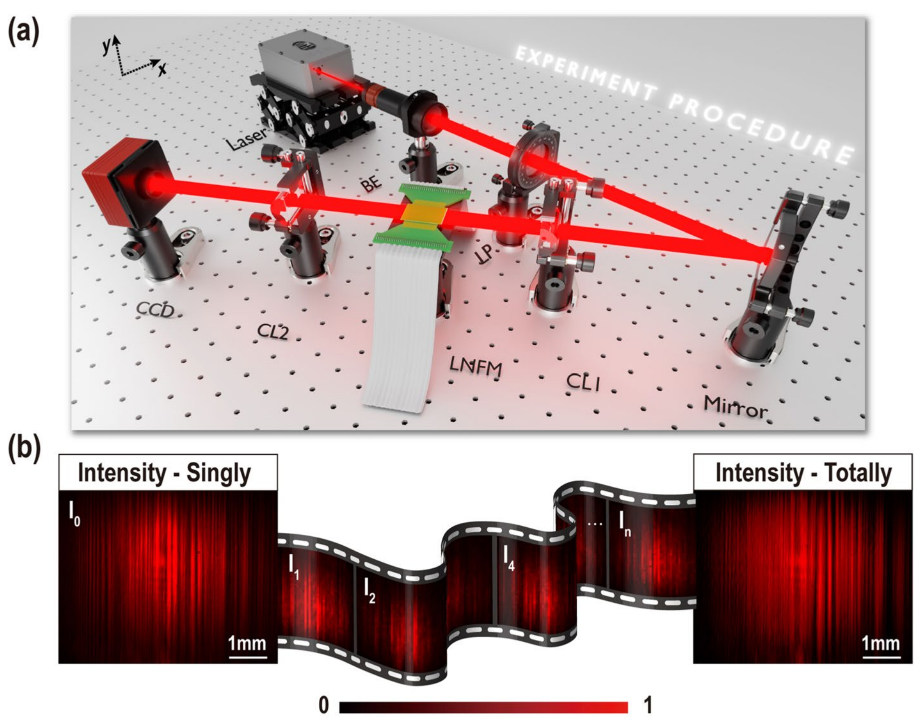

Fig. 3 Optical coherence manipulation experimental setup and results. **a** Experimental setup for high-speed optical coherence manipulation. BE, beam expander; LP, Linear polarizer; CL, cylindrical lens; LNFM, lithium niobate films modulator; CCD, charge-coupled device; **b** Experimental instantaneous intensity distributions and corresponding average intensity (rightmost) of 625 instantaneous intensities

digital micromirror devices and about 3000 times higher than the modulation rate of 8-bit grayscale values. Therefore, it is substantial to significantly increase the modulation rate of optical coherence manipulation through LNF modulator.

To verify the correlation nature of the generated sources, we utilize the Young's double-slit interference experiment to statistically measure the interference fringes of the beam in the far field, which reflects the spectral degree of coherence of the random fields [27]. More detailed description of the theoretical framework of the protocol is given in Supplementary Note 3. A depiction of which is shown in Fig. 4a, the generated beam illuminates onto a Young's two-pinhole mask, then the transmitted light is focused by a thin lens. Finally, a CCD detector captures the interference fringe at the focal plane (far field) of the thin lens. A high fringe contrast in the far field-better known as visibility-implies a coherent field, whereas a low fringe visibility implies incoherent light. The two-pinhole mask with 0.12 mm diameter holes and 0.6 mm separation is first used and this mask is placed at the source plane. Figure 4b shows the corresponding interference fringes and the calculated visibility $|\mu|$, one can see that the experimental results are in the reasonable agreement with the simulation coherence results, which indicate that

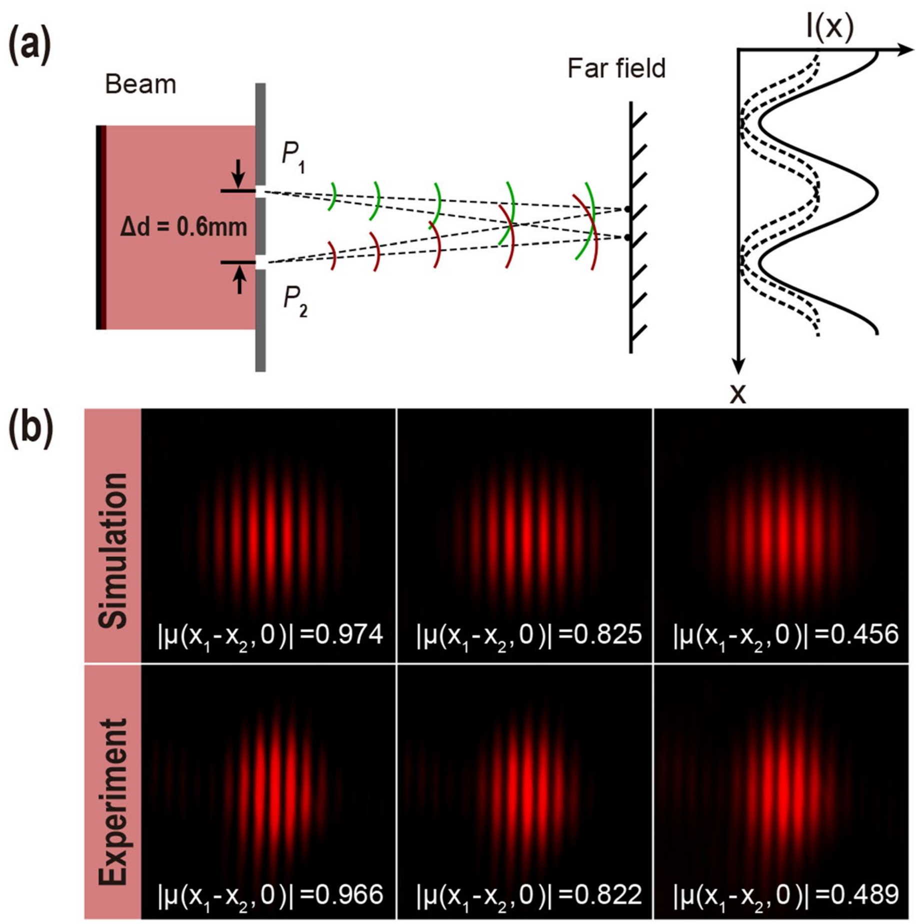

Fig. 4 Optical coherence measurement results. **a** Schematic of Young's interferometer depicted in the $x - z$ plane; **b** simulation (top) and experiment (bottom) results of observation-plane spectral density for different spectral degree of coherence

the generated fields comply with the statistical characteristics of partial coherence, and its coherence properties can be controlled with relative precision. Some differences may exist between the experimental and simulation results due to environmental noise, but these do not affect our ability to verify the control of optical coherence.

Discussion and conclusion

We propose an optical coherence manipulation strategy based on high-speed electro-optical modulation. Different voltage distributions are applied to the electrode channel of the LNF modulator to precisely control the refractive index difference, thereby achieving prescribed phase distribution loading of the wavefront. Using the linear driving voltage and phase transition relationship of LNF, we experimentally synthesized a random light field with a predefined optical coherence distribution. The experimental results are almost consistent with the theoretical predictions, achieving high-speed optical coherence manipulation. Compared with the method of controlling the coherence of light through traditional optical modulators, our method significantly improves the optical coherence manipulation rate while minimizing the energy loss of the incident light, which further promotes the practical application of optical coherence manipulation.

A random light field can be viewed as an incoherent superposition of coherent modes according to prescribed weights, and the phase element of each coherent mode contributes to their unique propagation features. Therefore, based on the above analysis, we can modify the coherence modes and weight distribution that constitute the random light source to modify the driving voltage distribution of the LNF modulator to achieve specific coherence customization of the light field through high-speed modulation. The proposed LNF modulator is limited by its one-dimensional structural design, restricting modulation to the one-dimensional optical coherence. The production of LNF modulator with two-dimensional spatial phase modulation capabilities will further promote the complex optical coherence manipulation. Our strategy paves the way for practical applications of optical coherence manipulation, such as information transmission and information retrieval in random media.

Methods

LNF modulator design and production. The proposed LNF modulator employs micro-nano processing techniques for electrode structure fabrication, including ultraviolet lithography, electron beam evaporation, and wire bonding. First, photoresist is spin-coated onto the cleaned LN crystal surface, and ultraviolet lithography is used to define the desired structural pattern. Next, a gold film is deposited onto the patterned photoresist using electron beam evaporation. Subsequently, acetone is utilized to dissolve the photoresist, resulting in the formation of a gold electrode array. Finally, the LN is affixed to the PCB circuit board, and the gold electrodes on the LN are electrically connected to the gold electrodes on the PCB circuit board through wire bonding. A more detailed description of the Fabrication processes of high-speed LNF modulator is given in Supplementary Note 1.

Supplementary Information

The online version contains supplementary material available at https://doi.org/10.1186/s43074-025-00176-5.

Supplementary Material 1: Supplementary information.

Acknowledgements
Not applicable.

Authors' contributions
Yangjian Cai, Xianfeng Chen, and Ya Cheng conceived the idea and supervise the research. Xinlei Zhu, Fengchao Ni, and Haigang Liu performed theoretical calculations and experimental measurements. Jiayi Yu and Fei Wang participated in the discussion. Yangjian Cai analyzed the results and polished the manuscript. All the authors discussed the contents and prepared the manuscript.

Authors' information
Not applicable.

Funding
National Natural Science Foundation of China (12192254, 12374276, 12304326, 92250304 and W2441005); National Key Research and Development Project of China (2022YFA1404800); China Postdoctoral Science Foundation (2022M721992); Natural Science Foundation of Shandong Province (ZR2023QA081).

Data availability
The datasets used and/or analysed during the current study are available from the corresponding author on reasonable request.

Declarations

Ethics approval and consent to participate
There is no ethics issue for this paper.

Consent for publication
All authors agreed to publish this paper.

Competing interests
The authors declare no competing financial interests.

Received: 11 December 2024 Revised: 2 June 2025 Accepted: 7 June 2025
Published online: 12 June 2025

References

1. Forbes A, de Oliveira M, Dennis MR. Structured light. Nat Photon. 2021;15:253–62.
2. Zhang Y, Wang Y, Wang M, Guo Y, Li X, Chen Y, et al. Multi-focus light-field microscopy for high-speed large-volume imaging. PhotoniX. 2022;3:30.
3. Qiao Z, Wan Z, Xie G, Wang J, Qian L, Fan D. Multi-vortex laser enabling spatial and temporal encoding. PhotoniX. 2020;1:1–14.
4. Goodman JW. Speckle Phenomena in Optics: Theory and Applications. Englewood: Roberts and Company Publishers; 2007.
5. Andrews L, Phillips R. Laser Beam Propagation Through Random Media. 2nd ed. Bellingham: SPIE; 2005.
6. Goodman JW. Statistical Optics. New York: Wiley; 2015.
7. Yu J, Zhu X, Wang F, Chen Y, Cai Y. Research progress on manipulating spatial coherence structure of light beam and its applications. Prog Quant Electron. 2023;91–92:100486.
8. Redding B, Choma MA, Cao H. Speckle-free laser imaging using random laser illumination. Nat Photon. 2012;6:355–9.
9. Peng Y, Choi S, Kim J, Wetzstein G. Speckle-free holography with partially coherent light sources and camera-in-the-loop calibration. Sci Adv. 2021;7:eabg5040.
10. Batarseh M, Sukhov S, Shen Z, Gemar H, Rezvani R, Dogariu A. Passive sensing around the corner using spatial coherence. Nat Commun. 2018;9:3629.
11. Lu X, Shao Y, Zhao C, Konijnenberg S, Zhu X, Tang Y, et al. Noniterative spatially partially coherent diffractive imaging using pinhole array mask. Adv Photon. 2019;1:016005.
12. Peng D, Huang Z, Liu Y, Chen Y, Wang F, Ponomarenko SA, Cai Y. Optical coherence encryption with structured random light. PhotoniX. 2021;2:1–15.
13. Liu Y, Dong Z, Zhu Y, Wang H, Wang F, Chen Y, Cai Y. Three-channel robust optical encryption via engineering coherence Stokes vector of partially coherent light. PhotoniX. 2024;5:8.
14. Yu J, Xu Y, Lin S, Zhu X, Gbur G, Cai Y. Longitudinal optical trapping and manipulating Rayleigh particles by spatial nonuniform coherence engineering. Phys Rev A. 2022;106:033511.
15. Zhao X, Wang Z, Lu X, Zhang H, Zhu J, Gao J, et al. Ultrahigh precision angular velocity measurement using frequency shift of partially coherent beams. Laser Photonics Rev. 2023;17:2300318.

16. Wolf E. Introduction to the Theory of Coherence and Polarization of Light. Cambridge: Cambridge University; 2007.
17. Wolf E. New theory of partial coherence in the space-frequency domain. Part I: Spectra and cross spectra of steady-state sources. J Opt Soc Am. 1982;72:343–51.
18. Liu L, Liu W, Wang F, Cheng H, Choi DY, Tian J, Cai Y, Chen S. Spatial coherence manipulation on the disorder-engineered statistical photonic platform. Nano Lett. 2022;22:6342–9.
19. Wooten EL, Kissa KM. A review of lithium niobate modulators for fber-optic communications systems. IEEE J Sel Top Quantum Electron. 2000;6:69.
20. Wang Y, Zhou S, He D, Hu Y, Chen H, Liang W, et al. Electro-optic beam deflection based on a lithium niobate waveguide with microstructured serrated electrodes. Opt Lett. 2016;41:4739.
21. Wang C, Zhang M, Chen X, Bertrand M, Shams-Ansari A, Chandrasekhar S, Loncar M. Integrated lithium niobate electro-optic modulators operating at CMOS-compatible voltages. Nature. 2018;562:101.
22. He M, Xu M, Ren Y, Jian J, Ruan Z, Xu Y, Liu L. High-performance hybrid silicon and lithium niobate Mach-Zehnder modulators for 100 Gbit s^{-1} and beyond. Nat Photonics. 2019;13:359.
23. Xu M, He M, Zhang H, Jian J, Cai X. High-performance coherent optical modulators based on thin-film lithium niobate platform. Nat Commun. 2020;11:3911.
24. Wolf E. Unified theory of coherence and polarization of random electromagnetic beams. Phys Lett A. 2003;312:263–7.
25. Wolf E, Collett E. Partially coherent sources which produce the same far-field intensity distribution as a laser. Opt Commun. 1978;25:293–6.
26. Wang F, Lv H, Chen Y, Cai Y, Korotkova O. Three modal decompositions of Gaussian Schell-model sources: comparative analysis. Opt Express. 2021;29:29676–89.
27. Gbur G, Visser TD. Young's interference experiment: Past, present, and future. Prog Opt. 2022;67:275–343.

Publisher's Note